




 Cite this: *RSC Adv.*, 2022, 12, 3892

Transformation of the coordination nanostructures of 4,4',4''-(1,3,5-triazine-2,4,6-triyl) tribenzoic acid molecules on HOPG triggered by the change in the concentration of metal ions†

 Sihao Li, Caimei Gong, Yuyang Zhang, Shizhang Fu, Zhongping Wang, Yan Lu, Siyi Gu, Xiaoqing Liu * and Li Wang *

The modulation effects of $\text{Cu}^{2+}/\text{Fe}^{3+}$ ions on the hydrogen-bonded structure of 4,4',4''-(1,3,5-triazine-2,4,6-triyl) tribenzoic acid (TATB) on a HOPG surface have been investigated at the liquid–solid interface by scanning tunneling microscopy (STM). STM observations directly demonstrated that the self-assembled honeycomb network of TATB has been dramatically transformed after introducing $\text{CuCl}_2/\text{FeCl}_3$ with different concentrations. The metal–organic coordination structures are formed due to the incorporation of the $\text{Cu}^{2+}/\text{Fe}^{3+}$ ions. Interestingly, a Cu^{2+} ion remains coordinated to two COOH groups and only the number of COOH groups involved in coordination doubles when the concentration of Cu^{2+} ions doubled. A Fe^{3+} ion changes from coordination to three COOH groups to two COOH groups after increasing the concentration of Fe^{3+} ions in a mixed solution. Such results suggest that the self-assembled structures of TATB molecules formed by metal–ligand coordination bonds can be effectively adjusted by regulating the concentration of metal ions in a mixed solution, which has rarely been reported before. It explains that the regulatory effect of concentration leads to the diversity of molecular architectures dominated by coordination bonds.

Received 15th December 2021

Accepted 22nd January 2022

DOI: 10.1039/d1ra09073a

rsc.li/rsc-advances

Introduction

Metal–organic coordination structures are materials comprising reticular metal centers and organic linkers in which the two constituents bind with each other *via* metal–ligand coordination interactions. The coordination-driven molecular self-assembly of nanostructures on solid surfaces has attracted much attention owing to the potential applications of such structures in nano-devices and nanopatterning in the future.^{1–4} Recently, coordination interaction has been used in the direct preparation of novel nanostructures ranging from clusters,^{5,6} 1D chains or polymers,^{7–10} to 2D coordination frameworks,^{11–14} and even 3D structures.^{15–17} Moreover, their composition, morphology and properties have been well proved, and have opened up specific and targeted application in the areas of chemical and materials sciences.^{18,19} However, few studies have focused on regulating the coordination structures which involves changing the metal species for coordination, and more importantly, the concentrations of metal ions used to form the coordination structures.

A variety of studies have demonstrated the coordination nanostructures by altering organic ligands, such as

carboxylate,^{3,5,12,18} hydroxyl,^{14,20,21} pyridine,^{9,22–25} and triazine.^{26–30} The triazine derivatives are important in a range of areas as ligands for supramolecular self-assembly of more complex mixed layers, hence it may be interesting to study the coordination properties of the triazine derivatives. In this article, we fabricated different coordination nanostructures by 4,4',4''-(1,3,5-triazine-2,4,6-triyl) tribenzoic acid (TATB) molecules coordinating with Cu^{2+} or Fe^{3+} ion with different concentrations on highly oriented pyrolytic graphite (HOPG) surface. Scanning tunneling microscopy (STM) images directly demonstrated the transformation of the nanostructure from self-assembled honeycomb networks formed by TATB molecules *via* hydrogen bonding into coordination nanostructures formed through the TATB molecules coordinated with metal ions. Moreover, by varying the concentrations of Cu^{2+} or Fe^{3+} ions, coordination structures with different shapes and sizes have been fabricated, which illustrates the concentrations and valence states of the metal ions plays important roles in the coordination nanostructures.

Experimental

Sample preparation

4,4',4''-(1,3,5-Triazine-2,4,6-triyl) tribenzoic acid (TATB) molecules used in this work weren't further purified after purchased from Ark Pharm. Ferric chloride and copper chloride were

Department of Physics, Nanchang University, Nanchang 330031, China. E-mail: liuxiaoqing@ncu.edu.cn; liwang@ncu.edu.cn

† Electronic supplementary information (ESI) available. See DOI: 10.1039/d1ra09073a



purchased from DAMAO. Stock solutions of 30 mL each of TATB and metal chloride were prepared by dissolving these reagents in nonanoic acid purchased from Aladdin. The concentrations of TATB, CuCl_2 and FeCl_3 were 2.2×10^{-5} M, 4.4×10^{-5} M and 5.8×10^{-6} M, respectively. The molar ratio of TATB to metal chloride in the final product was controlled by the deposited volumes. STM samples were prepared by dropping about 3.0 μL of the solutions on a freshly cleaved HOPG substrate. Then, the samples were kept at room temperature for about 0.5 h. Finally, the samples were investigated by STM at the liquid/solid interface.

STM measurements

The STM measurements were performed under atmospheric conditions, ambient temperature of about 25 °C. STM tips were made by cutting Pt/Ir (80/20) wire (California Fine Wire Co., Grover Beach, CA). All the STM images were acquired on a Pico-SPM (Molecular Imaging, Agilent Technology) scanning tunneling microscope operating in constant-current mode, the imaging parameters are stated in the figure captions, and extracted from raw data files using Pico Image Basic 6.2 program (Agilent, USA). To avoid possible experimental artifacts, each STM sample was repeatedly measured with different tips. The drift was calibrated using the underlying graphite lattice as a reference. High-resolution STM (HR-STM) images were low-pass-filtered.

Constructed and computational details

The above structures are calculated by first-principles density functional theory (DFT), as implemented in the Vienna *Ab initio* Simulation Package (VASP), with the PBE generalized-gradient exchange and correlation functional. A plane-wave basis set with a kinetic energy cutoff of 400 eV is adopted and the van der Waals interaction is considered with the optB86b-vdW method. A $1 \times 1 \times 1$ k -mesh was adopted for geometry optimization and total energy calculations. For structure relaxations, all atoms were fully relaxed until the residual force per atom was less than $0.02 \text{ eV } \text{\AA}^{-1}$.

Results and discussion

After depositing a droplet of nonanoic acid solution containing TATB molecules onto a freshly cleaved HOPG surface, STM images show that TATB molecules form a uniform monolayer with molecules lying flat on the surface. Fig. 1a shows the typical honeycomb network of TATB on HOPG. The high resolution STM image in Fig. 1b revealed that each TATB molecule has a three-clover structure, where each clover can be assigned to a benzoic acid moiety on the bridge arm of TATB. The group composed of six TATB molecules forms a hexagonal network, and the unit cell of the assembly is marked in Fig. 1b (rhomboid in white solid line). The vectors for the unit cell, a and b , is respectively of $(3.68 \pm 0.2) \text{ \AA}$ and $(3.68 \pm 0.2) \text{ \AA}$ and the angle α between the vectors is $(60 \pm 1^\circ)$. The proposed model of the supramolecular honeycomb network shown in Fig. 1c indicates that each TATB molecule can interact with three adjacent

molecules by the O–H \cdots O hydrogen bonds (as illustrated by yellow dashed lines in Fig. 1c). Simulated STM image in the Fig. 1d matches well with the STM result. We measured the distance of O–H \cdots O hydrogen bonds is approximately 2.64 \AA , which are in good agreement with the lengths as previously reported in organic crystals.³¹

When the nonanoic acid containing CuCl_2 and TATB (the molar ratio was adjusted to 1 : 2) is deposited on an HOPG surface, a well-ordered assembling structure composed of parallel chains labeled by white dotted line is found as shown in Fig. 2a, which is quite different from the honeycomb network composed of pure TATB molecules. Close examination in Fig. 2b reveals that these chains consist of some herringbone-like features and some dots. Since this structure only emerged after the introduction of CuCl_2 , these herringbone-like features and dots were attributed to TATB molecules and Cu^{2+} ions, respectively. The arrangement diagram of TATB molecules and Cu^{2+} was superimposed on Fig. 2b, in which the red graphics mark the distribution of TATB molecules and the light blue circles mark the arrangement of Cu^{2+} ions. Fig. 2c illustrates the corresponding optimized structure model. Two TATB molecules are bridged by Cu^{2+} ion to form coordination dimers, and the dimers are connected by two C–H \cdots O hydrogen bonds as illustrated by green dashed lines in Fig. 2c. Simulated STM images in Fig. 2d demonstrate that the C–H \cdots O hydrogen bond lengths are $(3.0 \pm 0.2) \text{ \AA}$ and the O–Cu–O coordination bond lengths are $(4.0 \pm 0.3) \text{ \AA}$, which is consistent with the STM result.

If we tune the molar ratio of CuCl_2 /TATB from 1 : 2 to 1 : 1, another parallel chain labeled by white dotted line were

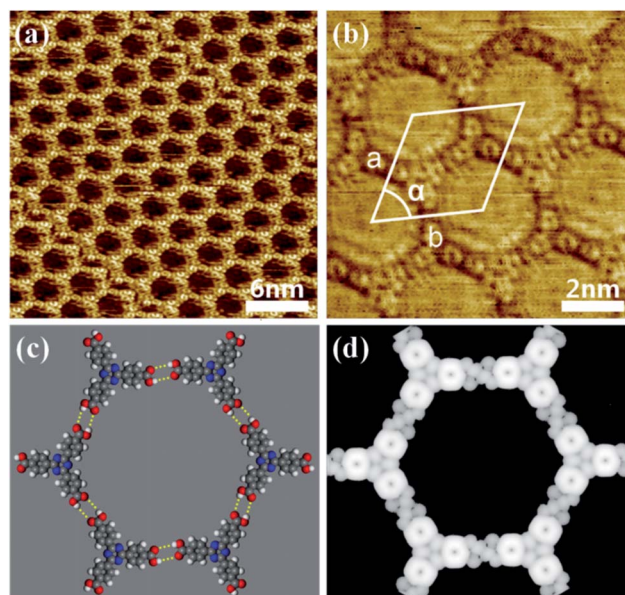


Fig. 1 The STM images and simulated STM images of TATB molecules on HOPG. (a) The large-scale STM image of self-assembly structure. Set point: $I = 0.5 \text{ nA}$, $V = -1 \text{ V}$. (b) High resolution STM image of honeycomb network. Set point: $I = 0.6 \text{ nA}$, $V = -0.8 \text{ V}$. (c) The fully relaxed model of the honeycomb network. Yellow dotted line: O–H \cdots O hydrogen bond. (d) Simulated STM image of (c).

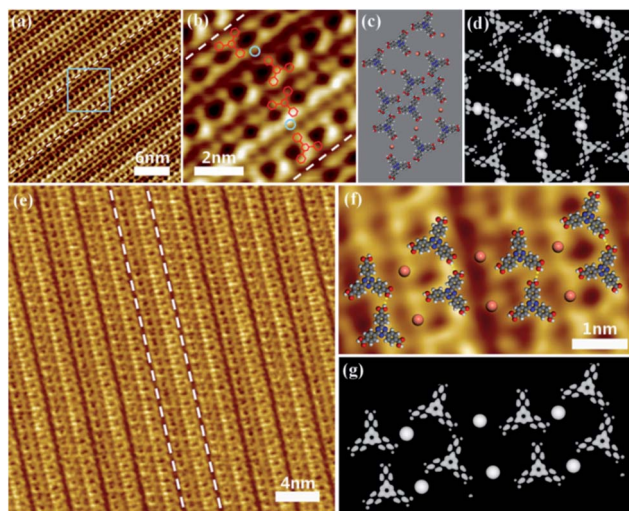


Fig. 2 (a) STM image of $\text{Cu}^{2+}/\text{TATB}$ ($\text{Cu}^{2+} : \text{TATB} = 1 : 2$) self-assembled chains on HOPG surface. Set point: $I = 0.55 \text{ nA}$, $V = -0.6 \text{ V}$. (b) The enlarged image of the area marked by the blue square in (a). The three-clover graphics label TATB molecules, and the blue circle represents the copper ions. (c) Schematic model of $1 : 2 \text{ Cu}^{2+}/\text{TATB}$ chain. (d) Simulated STM image of (c). (e) STM image of $\text{Cu}^{2+}/\text{TATB}$ ($\text{Cu}^{2+} : \text{TATB} = 1 : 1$) self-assembled structures on HOPG surface. Set point: $I = 0.57 \text{ nA}$, $V = -0.6 \text{ V}$. (f) High resolution STM image of $1 : 1 \text{ Cu}^{2+}/\text{TATB}$ chain superimposed with the schematic model. (g) Simulated STM image of (f). Blue dotted line: $\text{C}-\text{H}\cdots\text{O}$ hydrogen bond; yellow dotted line: $\text{O}-\text{H}\cdots\text{O}$ hydrogen bond.

obtained as shown in Fig. 2e. An overview image of the new chains reveals that such nanostructure is different with that above. Close examination in Fig. 2f reveals that these chains consist of some three-clover features and some dots. Similar to the above, these three-clover features and dots are designated as TATB molecules and Cu^{2+} ions, respectively. The optimized structure model superimposed on Fig. 2f illustrates two TATB molecules are bridged by Cu^{2+} ion to form coordination dimers, and the dimers on the same chain are connected by two $\text{O}-\text{H}\cdots\text{O}$ hydrogen bonds while the dimers on adjacent chains interact through $\text{O}-\text{Cu}-\text{O}$ coordination bond. The corresponding simulated STM image in Fig. 2g coincides well with the experimental STM image in Fig. 2f and shows that $\text{O}-\text{H}\cdots\text{O}$ hydrogen bond lengths are approximately $2.6 \pm 0.2 \text{ \AA}$ and $\text{O}-\text{Cu}-\text{O}$ coordination bond lengths are approximately $4.0 \pm 0.2 \text{ \AA}$, which confirms that the $\text{O}-\text{Cu}-\text{O}$ coordination bonds are the main driving force within the structure. Compared with the above chains, the dimers are also formed by $\text{O}-\text{Cu}-\text{O}$ coordination bond. However, the driving force between the dimers on the adjacent chain changes from $\text{C}-\text{H}\cdots\text{O}$ hydrogen bond into $\text{O}-\text{Cu}-\text{O}$ coordination bond, which results to the transformation of self-assembly structure of the chains. The result shows that the polymorphic self-assembly of TATB molecules and Cu^{2+} is realized on HOPG by increasing the concentration of metal ions.

Similar structural transformation was obtained by depositing a mixed solution of TATB molecules and FeCl_3 on HOPG. Fig. 3a shows the typical STM image of the assembled structure

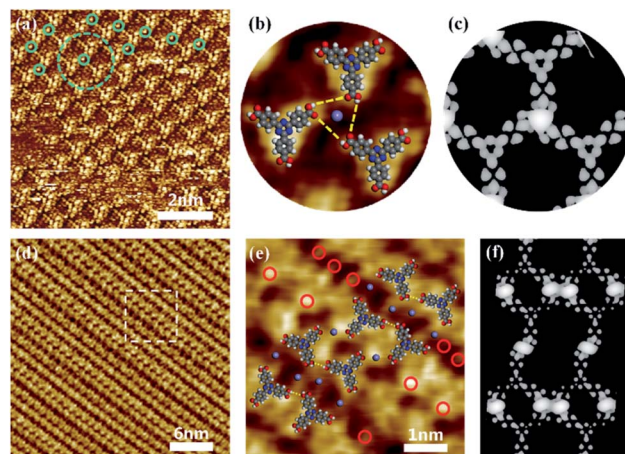


Fig. 3 (a) STM image of $\text{Fe}^{3+}/\text{TATB}$ ($\text{Fe}^{3+} : \text{TATB} = 1 : 1$) self-assembled line network on HOPG surface. Fe ions in the STM image is marked with a solid green circle. Set point: $I = 0.7 \text{ nA}$, $V = -0.8 \text{ V}$. (b) The enlarged image of the area denoted by the green circle in (a) superimposed with the schematic model of TATB/ Fe^{3+} trimers. (c) Simulated STM images of (b). (d) STM image of $\text{Fe}^{3+}/\text{TATB}$ ($\text{Fe}^{3+} : \text{TATB} = 3 : 2$) self-assembled chains on HOPG surface. Set point: $I = 0.7 \text{ nA}$, $V = -0.6 \text{ V}$. (e) The enlarged image and schematic model of the ($\text{Fe}^{3+} : \text{TATB} = 3 : 2$) chain in the white square of (d). Fe ions in the STM image is marked with a solid red circle. Yellow dashed line: $\text{O}-\text{H}\cdots\text{O}$ hydrogen bond. (f) Simulated STM images of (e).

formed by depositing a mixture of TATB molecules and FeCl_3 with a molar ratio of $1 : 1$ on the HOPG surface. The estimated coverage of iron on the surface is about $1.67 \text{ ion per nm}^2$. It can be seen that the building blocks for the structure are the trimers of TATB molecules in which one bright dot is surrounded by three bright clover-shaped structures with a local threefold symmetry as marked by a green dotted circle in Fig. 3a. As the proposed model superimposed on the STM image in Fig. 3b, the central small bright spot is attributed to Fe^{3+} and the three clover-shaped bright spots represents three TATB molecules. In this model of TATB/ Fe^{3+} trimers, three carboxyl groups linked with one Fe^{3+} ion through metal coordination, and the three carboxyl groups are connected to each other through $\text{O}-\text{H}\cdots\text{O}$ hydrogen bonds. The corresponding simulated STM image in Fig. 3c is consistent with the experimental STM image in Fig. 3b and shows that the length of three $\text{Fe}-\text{O}$ coordination bonds between three oxygen atoms within the carboxyl groups of TATB molecules and the centered Fe^{3+} ion are 2.110 \AA , 2.089 \AA and 2.106 \AA respectively, which is in good agreement with typical length of $\text{Fe}-\text{O}$ bond in previous studies.

After adjusting the molar ratio of $\text{FeCl}_3 : \text{TATB}$ to $3 : 2$, the self-assembly structure of TATB molecules and Fe^{3+} ions have undergone an obvious change from trimer structure to chain structure (Fig. 3d). Close examination in Fig. 3e allows us to propose the structure model: TATB molecules between adjacent chains interact *via* $\text{O}-\text{Fe}-\text{O}$ coordination bond, while TATB molecules on the same chain are contact with each other by $\text{O}-\text{H}\cdots\text{O}$ hydrogen bonds. In the Fig. 3e, Fe^{3+} ions are marked by small brown dots and red circles, and TATB molecules are presented with optimized structural formulas. Obviously, $\text{O}-\text{Fe}-$

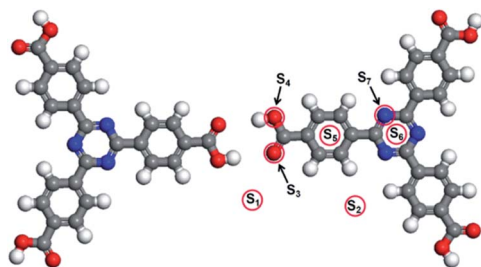


Fig. 4 Seven potential sites (S_1 , S_2 , S_3 , S_4 , S_5 , S_6 and S_7) of $\text{Cu}^{2+}/\text{Fe}^{3+}$ adsorbed on TATB dimer.

O coordination bond plays a dominant role in the assembly structure. It is worth noting that one Fe^{3+} ion coordinates with two carboxyl groups instead of three carboxyl groups mentioned above, as a consequence, the self-assembly structure of TATB and FeCl_3 changes from network into chain. Fig. 3f shows the corresponding simulated STM image obtained by DFT calculation.

The DFT calculation provides an insight into the adsorption of Cu^{2+} or Fe^{3+} ion in the self-assembled structures of TATB molecules *via* metal–organic coordination bonding. Fig. 4 illustrates seven potential sites of metal adsorbed on TATB dimer and the DFT results for seven adsorption sites are listed in Table 1. The corresponding optimized structure models and STM simulation images are shown in ESI Fig. 1 and 2.† In the system of $\text{Cu}^{2+}/\text{Fe}^{3+}$ and TATB dimer, the lowest total energy is E_{S_7} and E_{S_5} , respectively, indicating that the best adsorption site of Cu^{2+} is S_7 and that of Fe^{3+} is S_5 . On this basis, DFT calculations are performed on four systems with multiple potential configurations according to our experimental system mentioned above as shown in Fig. 5. The DFT results demonstrate that the configurations S_4 , S_8 , S_{12} and S_{16} have the lowest total energy of -1359.54 eV, -1362.14 eV, -686.99 eV and -692.16 eV in the system with the molar ratio $\text{Cu}^{2+}/\text{TATB}$ of 1 : 2, $\text{Cu}^{2+}/\text{TATB}$ of 1 : 1, $\text{Fe}^{3+}/\text{TATB}$ of 1 : 1 and $\text{Fe}^{3+}/\text{TATB}$ of 3 : 2, respectively. Comparing several configurations in each system, it is easy to find that $\text{Cu}^{2+}/\text{Fe}^{3+}$ ions are all coordinated with TATB molecules in configurations S_4 , S_8 , S_{12} and S_{16} rather than one or more $\text{Cu}^{2+}/\text{Fe}^{3+}$ ions only adsorbed on TATB molecules in other configurations. Significantly, the configuration in S_4 , S_8 , S_{12} and S_{16} is in good agreement with the corresponding model proposed in each system, which further proves the correctness of our proposed model.

Table 1 Calculated total system energy for single Cu^{2+} or Fe^{3+} ion adsorbed on TATB dimer at different sites. Energy unit: eV

Energy	Cu	Fe
E_{S_1}	-678.26	-681.18
E_{S_2}	-678.35	-679.2
E_{S_3}	-678.73	-680.86
E_{S_4}	-678.410	-682.35
E_{S_5}	-678.00	-682.38
E_{S_6}	-678.33	-681.63
E_{S_7}	-679.18	-681.64

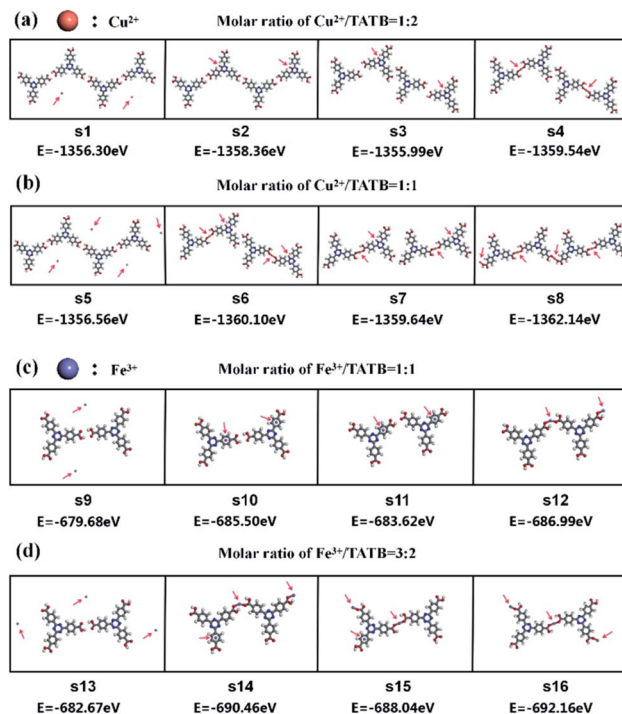


Fig. 5 DFT calculation results of the total energy for the system of $\text{Cu}^{2+}/\text{Fe}^{3+}$ and TATB dimer. (a) The total system energy for 1 : 2 $\text{Cu}^{2+}/\text{TATB}$ structure. (b) The total system energy for 1 : 1 $\text{Cu}^{2+}/\text{TATB}$ structure. (c) The total system energy for 1 : 1 $\text{Fe}^{3+}/\text{TATB}$ structure. (d) The total system energy for 3 : 2 $\text{Fe}^{3+}/\text{TATB}$ structure. The red arrows indicate the sites of Cu^{2+} or Fe^{3+} ions.

Conclusions

The self-assembled hydrogen-bonded molecular network of TATB has been dramatically transformed after introducing $\text{CuCl}_2/\text{FeCl}_3$ with different concentrations. The deposited monolayer of TATB molecules shows honeycomb structure. The $\text{Cu}^{2+}/\text{Fe}^{3+}$ ions can incorporate with TATB molecule *via* metal–organic coordination to form new structures, and the self-assembled structures of TATB molecules on HOPG formed by metal–ligand coordination bond can be effectively adjusted by tuning the concentration of metal ions in mixed solution.

Author contributions

X. L. and L. W. conceived and designed the experiment, discussed and analyzed data, and wrote the manuscript. S. L. and X. L. performed sample preparation and STM. S. L., S. G., X. L., Y. Z. and Z. W. analyzed the data. S. L., S. F., C. G., and Y. L. performed the DFT calculations and theoretical analyses. All authors discussed the results and commented on the manuscript.

Conflicts of interest

There are no conflicts to declare.

Acknowledgements

This work was financially supported by National Natural Science Foundation of China (Grant No. 11727902, 61864007, 22162018, 61927813 and 11774341) and Natural Science Foundation of Jiangxi Province (20202BABL203013).

Notes and references

- 1 S. Xing, Z. Zhang, X. Fei, W. Zhao, R. Zhang, T. Lin, D. Zhao, H. Ju, H. Xu, J. Fan, J. Zhu, Y. Q. Ma and Z. Shi, *Nat. Commun.*, 2019, **10**, 70.
- 2 T. Sirtl, S. Schlogl, A. Rastgoo-Lahrood, J. Jelic, S. Neogi, M. Schmittel, W. M. Heckl, K. Reuter and M. Lackinger, *J. Am. Chem. Soc.*, 2013, **135**, 691–695.
- 3 W. Li, J. Jin, X. Leng, Y. Lu, X. Liu and L. Wang, *J. Phys. Chem. C*, 2016, **120**, 12605–12610.
- 4 X. Qiu, X. Xiang, T. Liu, H. Huang and Y. Hu, *Process Biochem.*, 2020, **95**, 47–54.
- 5 Q. Li, L. Yan, Z. Wang, Y. Lu, S. Wei, X. Liu and L. Wang, *J. Chem. Phys.*, 2020, **152**, 044704.
- 6 X. Meng, E. Kolodzeiski, X. Huang, A. Timmer, B. Schulze Lammers, H. Y. Gao, H. Mönig, L. Liu, W. Xu, S. Amirjalayer, D. Zhu and H. Fuchs, *ChemNanoMat*, 2020, **6**, 1479–1484.
- 7 M. Telychko, J. Su, A. Gallardo, Y. Gu, J. I. Mendieta-Moreno, D. Qi, A. Tadich, S. Song, P. Lyu, Z. Qiu, H. Fang, M. J. Koh, J. Wu, P. Jelinek and J. Lu, *Angew. Chem., Int. Ed.*, 2019, **58**, 18591–18597.
- 8 J. F. Schultz, B. Yang and N. Jiang, *J. Chem. Phys.*, 2021, **154**, 044703.
- 9 S. Xing, Z. Zhang, H. Liang, B. Sun, H. Xu, J. Fan, Y. Q. Ma and Z. Shi, *Langmuir*, 2020, **36**, 6286–6291.
- 10 J. Li, L. Solianyky, N. Schmidt, B. Baker, S. Gottardi, J. C. Moreno Lopez, M. Enache, L. Monjas, R. van der Vlag, R. W. A. Havenith, A. K. H. Hirsch and M. Stohr, *J. Phys. Chem. C*, 2019, **123**, 12730–12735.
- 11 Y. Guo, A. Nuermaiti, N. D. Kjeldsen, K. V. Gothelf and T. R. Linderoth, *J. Am. Chem. Soc.*, 2020, **142**, 19814–19818.
- 12 A. Dmitriev, H. Spillmann, N. Lin, J. V. Barth and K. Kern, *Angew. Chem.*, 2003, **115**, 2774–2777.
- 13 C. Wäckerlin and K.-H. Ernst, *J. Phys. Chem. C*, 2021, **125**, 13343–13349.
- 14 A. Rochefort, L. Vernisse, A. C. Gómez-Herrero, C. Sánchez-Sánchez, J. A. Martín-Gago, F. Chérioux, S. Clair, J. Coraux and J. I. Martínez, *J. Phys. Chem. C*, 2021, **125**, 17333–17341.
- 15 L. Shao, B. Hua, X. Hu, D. Stalla, S. P. Kelley and J. L. Atwood, *J. Am. Chem. Soc.*, 2020, **142**, 7270–7275.
- 16 L. Shao, X. Hu, K. Sikligar, G. A. Baker and J. L. Atwood, *Acc. Chem. Res.*, 2021, **54**, 3191–3203.
- 17 Y. Jin, Q. Zhang, Y. Zhang and C. Duan, *Chem. Soc. Rev.*, 2020, **49**, 5561–5600.
- 18 S. O. Parreiras, D. Moreno, B. Cirera, M. A. Valbuena, J. I. Urgel, M. Paradinas, M. Panighel, F. Ajejas, M. A. Nino, J. M. Gallego, M. Valvidares, P. Gargiani, W. Kuch, J. I. Martinez, A. Mugarza, J. Camarero, R. Miranda, P. Perna and D. Eciija, *Small*, 2021, e2102753.
- 19 X. Bi, Y. Zhang, F. Zhang, S. Zhang, Z. Wang and J. Jin, *ACS Appl. Mater. Interfaces*, 2020, **12**, 49101–49110.
- 20 X. Chen, L. Shang, H. Cui, H. Yang, L. Liu, Y. Ren and J. Wang, *CrystEngComm*, 2020, **22**, 5900–5913.
- 21 U. Manna and G. Das, *Coord. Chem. Rev.*, 2021, **427**, 213547.
- 22 V. Velasco, D. Aguila, L. A. Barrios, I. Borilovic, O. Roubeau, J. Ribas-Arino, M. Fumanal, S. J. Teat and G. Aromi, *Chem. Sci.*, 2015, **6**, 123–131.
- 23 A. Rajput and R. Mukherjee, *Coord. Chem. Rev.*, 2013, **257**, 350–368.
- 24 D. Urankar, B. Pinter, A. Pevec, F. De Proft, I. Turel and J. Kosmrlj, *Inorg. Chem.*, 2010, **49**, 4820–4829.
- 25 T. R. Umbach, M. Bernien, C. F. Hermanns, L. L. Sun, H. Mohrmann, K. E. Hermann, A. Krüger, N. Krane, Z. Yang, F. Nickel, Y.-M. Chang, K. J. Franke, J. I. Pascual and W. Kuch, *Phys. Rev. B: Condens. Matter Mater. Phys.*, 2014, **89**, 235409.
- 26 N. Shekarlab, R. Ghorbani-Vaghei and S. Alavinia, *J. Organomet. Chem.*, 2021, **949**, 121971.
- 27 N. Portolés-Gil, A. M. López-Periago, A. Borrás, J. Fraile, E. Solano, O. Vallcorba, J. G. Planas, J. A. Ayllón and C. Domingo, *Cryst. Growth Des.*, 2020, **20**, 3304–3315.
- 28 T. Schäfer, A. E. Sedykh, J. Becker and K. Müller-Buschbaum, *Z. Anorg. Allg. Chem.*, 2020, **646**, 1555–1562.
- 29 S. Rajak, M. Mohan, A. A. Tremblay, T. Maris, S. Leal do Santos, E. C. Venancio, S. Ferreira Santos and A. Duong, *ACS Omega*, 2019, **4**, 2708–2718.
- 30 F. Marandi, K. Moeini, B. Mostafazadeh and H. Krautscheid, *Polyhedron*, 2017, **133**, 146–154.
- 31 T. Steiner, *Angew. Chem. Int. Ed.*, 2002, **41**, 48–76.